International Journal of Material Forming (2022) 15:59
https://doi.org/10.1007/s12289-022-01705-4

30TH ANNIVERSARY OF THE KOREAN SOCIETY FOR TECHNOLOGY OF PLASTICITY

Analysis of damage and fracture behavior in ductile metal sheets undergoing compression and shear preloading

Moritz Zistl[1] · Michael Brünig[1] · Steffen Gerke[1]

Received: 21 February 2022 / Accepted: 7 June 2022
© The Author(s) 2022

Abstract
The present paper comprises the experimental and numerical analysis of damage and fracture behavior of ductile metals under non-proportional loading with compression and shear preloading. For this purpose, biaxial experiments with the H-specimen using a pneumatic downholder for compression loading followed by failure under a tension stress state and corresponding numerical simulations are performed and analyzed. A thermodynamically consistent anisotropic continuum model is presented. It takes the effects of micromechanical damage mechanisms on the macro scale behavior as a motivation for a phenomenological description of damage behavior as a function of stress state. The experimental findings are compared with the results of tests with proportional load paths and corresponding numerical simulations. Thereto, strain fields of the critical areas of the specimens are analyzed by means of digital image correlation (DIC) technique. Compression and shear preloading can lead to significantly reduced ductility of the material with initiation of failure processes in the small damage strain range. Evolution of numerically predicted plastic and damage equivalent strains illustrates their stress state dependence. The numerical results are also confirmed by images of fracture surfaces taken by scanning electron microscopy (SEM). This experimental-numerical methodology is therefore an efficient tool to develop and validate general modeling approaches, and it is characterized by almost arbitrarily definable load paths with changes in stress states occurring in forming processes.

Keywords Ductile damage and fracture · Stress state dependence · Load path dependence · Biaxial experiments · Numerical simulations

Introduction

A considerable challenge in engineering production processes is the prediction of ductile material failure. In these processes, multiaxial and non-proportional loading types are present but are often not taken into account in numerical modeling. They require detailed knowledge of the material behavior under the expected loading conditions. For sheet metals in multi-stage forming processes, for example, this includes information regarding the localization tendencies, irreversible strains, damage and fracture under a wide variety of loading conditions.

Furthermore, a strong influence of the load path on damage evolution and failure processes has been observed in several experiments and engineering applications. This effect is especially difficult to address for sheet metals undergoing high compression and shear loading due to buckling of the specimens. Consequently, reliable experimental methods, including various loading conditions and non-proportional loading, are needed for material characterization. In this context, the development of accurate and practically applicable material models addressing the stress state dependency of damage and failure mechanisms is essential. The stress state therein is often characterized by the stress triaxiality and the Lode parameter.

This article belongs to the Topical Collection: *30th Anniversary of the Korean Society for Technology of Plasticity*

Guest Editors: Frederic Barlat, Jeong-Whan Yoon

✉ Moritz Zistl
moritz.zistl@unibw.de

Michael Brünig
michael.bruenig@unibw.de

Steffen Gerke
steffen.gerke@unibw.de

[1] Institut für Mechanik und Statik, Universität der Bundeswehr München, Werner-Heisenberg-Weg 39, 85577 Neubiberg, Germany

Published online: 02 July 2022

Two main approaches have been established to analyze and calibrate these dependencies. First, micro-mechanical simulations can be used to investigate the individual behavior of micro-defects in unit cells under a variety of loading conditions with the corresponding stress states and to study in detail the effects of coalescence leading to macro-cracks in the further deformation process [1–4]. On the other hand, since the spatial distribution and the size of defects in a metal structure have a random nature, it is difficult to transfer the results of an only numerical description to a real production process. Therefore, the influence of damage mechanisms under different stress conditions on the deformation and failure behavior is being investigated experimentally.

For this purpose, various experiments are usually performed with different unnotched and notched uniaxially loaded specimens [5–9]. A disadvantage of these tests is the small range of covered stress states. The experimental program can be extended by using carefully designed specimens with different modes of operation or undergoing combined biaxial loading conditions leading to a wide range of different stress states [10–17]. Experimental extension devices have been developed in order to avoid buckling under shear and compression loading [18–20].

Several experimental studies have focused on non-proportional load paths with a sudden change in stress state. An abrupt change in the load path can be achieved by predeforming unnotched tensile specimens in the first load step. The stress state of the deformed specimens is then changed for the second load step by subsequently incorporated notches [21–23]. However, most actual structures are subjected to loads during the component life cycle that are random or characterized by a smooth change. Therefore, a sudden change in stress state and also the alteration or introduction of residual stresses by the machining process must be viewed very critically. Furthermore, changes in stress states can occur in sequentially loaded specimens with a corresponding special test apparatus through loading in different directions of the specimen. Here, for example, the non-proportional loading is accomplished by sequentially alternating tension or compression and torsion stress states [24–27]. For tubes or hollow cylindrical specimens, tension stress states and internal compression stresses can be investigated [28, 29]. Studies with shear stress states [25, 30] have also been conducted to investigate the influence of load paths on evolution of damage and failure. A general trend found in these studies is that fracture strains strongly depend on the load path and that changes in local stress states occasionally result in slightly increased ductility, but usually in decreased ductility. Ordinary cruciform specimens have been used [31, 32] to study the load path dependence of the ductile damage and fracture processes on central cracks manufactured with different inclinations. A recently proposed approach is the use of biaxial specimens [12] made of sheets, in which the ratio of axis loading can be changed in defined ways, and thus the stress states in critical regions of the specimen can be varied sequentially and by superimposed loadings [33–35]. This method is characterized by a wide range of possible variations in the individual stress states as well as in the design of non-proportional load paths [36, 37].

In the present paper, based on former investigations by the authors [36, 37], a new series of experiments with non-proportional load cases with changes from compression and shear loading to tension dominated stress states with the H-specimen and a new downholder apparatus preventing buckling are proposed. A phenomenological continuum model using stress-state-dependent damage mode functions to describe the effects of micro-scale damage evolution on the macro-scale level is briefly discussed. Experimental results for the aluminum alloy EN AW 6082-T6 including load-displacement data, strain fields reported by digital image correlation, images of the fracture surfaces obtained by scanning electron microscopy and numerical results of corresponding numerical simulations of the biaxial experiments are presented. Based on these results, the load path dependency of damage and failure mechanisms under shear and compression preloading can be shown. Furthermore, the used constitutive model is able to accurately predict the complex material behavior. The validity of the experimental-numerical methodology for non-proportional compression loading of metal sheets is elucidated.

Continuum damage model

To describe the damage and failure behavior of ductile metals, the model of Brünig [38, 39] is used. The analysis of inelastic deformations in this phenomenological framework takes into account experimental and numerical investigations on both the micro- and macro-levels, taking into account different processes on these scales and their interactions [4, 40]. It is based on the introduction of the damage strain tensor, $\mathbf{A}^{\mathrm{da}}$, characterizing the macroscopic strain behavior caused by the evolution of damage mechanisms on the micro-scale. The appearance of these micro-mechanisms is strongly dependent on the present stress state [41, 42]. A series of multiaxial experiments with different loading histories covering wide range of stress states is necessary in order to propose and validate evolution equations for these different stress-state-dependent mechanisms as well as to identify corresponding parameters.

The continuum approach considers damaged as well as fictitious undamaged configurations with effective quantities, see [38, 39] for further details. It is based on the strain rate tensor derived from the Oldroyd rate of the metric transformation tensor and is additively decomposed into elastic, $\dot{\mathbf{H}}^{\mathrm{el}}$, effective plastic, $\dot{\mathbf{H}}^{\mathrm{pl}}$, and damage parts, $\dot{\mathbf{H}}^{\mathrm{da}}$ and

Considering the undamaged configurations, the effective Kirchhoff stress tensor is introduced

$$\bar{\mathbf{T}} = 2G\mathbf{A}^{\mathrm{el}} + \left(K - \frac{2}{3}G\right)\mathrm{tr}\mathbf{A}^{\mathrm{el}}\mathbf{1} \tag{1}$$

with the elastic strain tensor $\mathbf{A}^{\mathrm{el}}$ and G and K represent the shear and bulk modulus.

Plastic behavior of ductile metals is defined in the undamaged configurations without influence of damage degradation. It is characterized by the yield criterion

$$f^{\mathrm{pl}}\left(\bar{J}_2, c\right) = \sqrt{\bar{J}_2} - c = 0, \tag{2}$$

expressed in terms of the second deviatoric invariant of the effective stress tensor (1), $\bar{J}_2 = \frac{1}{2}\mathrm{dev}\bar{\mathbf{T}} \cdot \mathrm{dev}\bar{\mathbf{T}}$ and the equivalent yield stress c of the undamaged material. Plastic hardening

$$c = c_o + R_\infty\left(1 - e^{-b\gamma}\right) \tag{3}$$

is described by the Voce law [43] with the initial yield stress c_o, the hardening modulus R_∞ and the hardening exponent b. The effective plastic strain rate

$$\dot{\bar{\mathbf{H}}}^{\mathrm{pl}} = \dot{\lambda}\frac{1}{2\sqrt{\bar{J}_2}}\mathrm{dev}\bar{\mathbf{T}} = \dot{\gamma}\bar{\mathbf{N}}. \tag{4}$$

predicts the evolution of isochoric plastic deformations where $\dot{\lambda}$ denotes a non-negative scalar factor, $\bar{\mathbf{N}} = \left(1/\sqrt{2\bar{J}_2}\right)\mathrm{dev}\bar{\mathbf{T}}$ is the normalized deviatoric effective stress tensor and $\dot{\gamma} = \bar{\mathbf{N}} \cdot \dot{\bar{\mathbf{H}}}^{\mathrm{pl}} = \frac{1}{\sqrt{2}}\dot{\lambda}$ represents the equivalent plastic strain rate.

Furthermore, damaged configurations are considered where the Kirchhoff stress tensor

$$\begin{aligned}\mathbf{T} = {} & 2\left(G + \eta_2\mathrm{tr}\mathbf{A}^{\mathrm{da}}\right)\mathbf{A}^{\mathrm{el}} + \Big[\eta_3\left(\mathbf{A}^{\mathrm{da}} \cdot \mathbf{A}^{\mathrm{el}}\right) \\ & + \left(K - \tfrac{2}{3}G + 2\eta_1\mathrm{tr}\mathbf{A}^{\mathrm{da}}\right)\mathrm{tr}\mathbf{A}^{\mathrm{el}}\Big]\mathbf{1} \\ & + \eta_3\mathrm{tr}\mathbf{A}^{\mathrm{el}}\mathbf{A}^{\mathrm{da}} + \eta_4\left(\mathbf{A}^{\mathrm{el}}\mathbf{A}^{\mathrm{da}} + \mathbf{A}^{\mathrm{da}}\mathbf{A}^{\mathrm{el}}\right)\end{aligned} \tag{5}$$

depends on both the elastic and the damage strain tensors, $\mathbf{A}^{\mathrm{el}}$ and $\mathbf{A}^{\mathrm{da}}$, to take into account material deterioration caused by damage evolution described by the additional material parameters $\eta_1 ... \eta_4$. It should be noted that as long as the material remains undamaged $\mathbf{A}^{\mathrm{da}} = \mathbf{0}$, the stress tensor (5) is equivalent to the effective one (1).

The stress state can be characterized by the stress triaxiality

$$\eta = \frac{\sigma_{\mathrm{m}}}{\sigma_{\mathrm{eq}}} = \frac{I_1}{3\sqrt{3J_2}} \tag{6}$$

defined as the ratio of the mean stress σ_m and the von Mises equivalent stress σ_{eq} or, alternatively, by the first and second deviatoric invariants of the Kirchhoff stress tensor (5), $I_1 = \mathrm{tr}\mathbf{T}$ and $J_2 = \frac{1}{2}\mathrm{dev}\mathbf{T} \cdot \mathrm{dev}\mathbf{T}$. The stress state is additionally described by the Lode parameter

$$\omega = \frac{2T_2 - T_1 - T_3}{T_1 - T_3} \quad \text{with} \quad T_1 \geq T_2 \geq T_3 \tag{7}$$

written in terms of the principal Kirchhoff stress components T_1, T_2 and T_3.

The damage process is governed by the damage condition

$$f^{\mathrm{da}} = \alpha I_1 + \beta\sqrt{J_2} - \sigma = 0 \tag{8}$$

defining the onset of damage behavior with the equivalent damage stress σ. The stress-state-dependent factors α and β represent damage mode parameters corresponding to the different damage processes acting on the micro-scale. In particular, tensile loading with high positive stress triaxialities leads to nucleation and growth of micro-voids followed by their coalescence, whereas during shear and compressive loading with small positive or negative stress triaxialities formation and growth of micro-shear-cracks leading to their coalescence are the main processes. A combination of these basic damage mechanisms on the micro-scale is active for moderate positive stress triaxialities and no damage formation has been observed in ductile metals for high negative stress triaxialities. The damage softening

$$\sigma = \sigma_o - H_1\mu^2 \tag{9}$$

is described by a quadratic function with the initial damage stress σ_o and the softening modulus H_1.

$$\dot{\mathbf{H}}^{\mathrm{da}} = \dot{\mu}\left(\hat{\alpha}\frac{1}{\sqrt{3}}\mathbf{1} + \hat{\beta}\tilde{\mathbf{N}} + \hat{\delta}\tilde{\mathbf{M}}\right) \tag{10}$$

In addition, the damage strain rate tensor is introduced which phenomenologically describes the evolution of irreversible macroscopic strains caused by the aforementioned different damage processes on the micro-scale. In Eq. 10 $\dot{\mu}$ denotes the equivalent damage strain rate and $\tilde{\mathbf{N}} = \left(1/\sqrt{2J_2}\right)\mathrm{dev}\tilde{\mathbf{T}}$ and $\tilde{\mathbf{M}} = \mathrm{dev}\tilde{\mathbf{S}}/||\mathrm{dev}\tilde{\mathbf{S}}||$ are the normalized stress-state-related deviatoric tensors with

$$\mathrm{dev}\tilde{\mathbf{S}} = \mathrm{dev}\tilde{\mathbf{T}}\mathrm{dev}\tilde{\mathbf{T}} - \frac{2}{3}J_2\mathbf{1} \tag{11}$$

where $\tilde{\mathbf{T}}$ represents the stress tensor work-conjugate to the damage strain rate tensor (10), see [38] for further details. In Eq. 10 the kinematic parameters $\hat{\alpha}$, $\hat{\beta}$ and $\hat{\delta}$ characterize the fraction of volumetric and isochoric deformations corresponding to the different stress-state-dependent damage and failure

mechanisms on the micro-level (evolution of micro-voids as well as evolution of micro-shear-cracks).

Numerical studies on the micro-scale analyzing deformation and failure behavior of differently loaded micro-defect-containing representative volume elements [4] have been performed to identify functions of the damage mode parameters α and β in Eq. 8 as well as $\hat{\alpha}$, $\hat{\beta}$ and $\hat{\delta}$ in Eq. 10. Since they are only based on numerical analysis, they have to be validated by experiments undergoing a wide range of stress states. In this context, experimental series with shear and tensile stress states in non-proportional loading have already been investigated [33, 34, 36, 37], whereas stress states with negative triaxialities and their influence on non-proportional loading previously have not been possible due to the experimental difficulties with compressive loading and buckling of metal sheets. The present work addresses these difficulties and extends those investigations.

Methodology

Experimental setup

The experiments are performed with the biaxial test machine type LFM-BIAX 20kN (produced by Walter & Bai, Switzerland). It consists of four electro-mechanically driven actuators with load maxima of $\pm 20kN$ and has a spindle stroke of 200mm (Fig. 1a). The specimens are clamped into the four heads of the actuators and then strained biaxially with different load paths. The experimental control technique is described in detail in [12, 34] for proportional loading and non-proportional loading, respectively. As a result, three cylinders are moving displacement controlled (at 0.004mm/s) and the displacements of opposite cylinders remain symmetrical with a constant load ratio.

When using thin specimens with compression loading, out-of-sheet-plane deformations must be avoided. Therefore, a pneumatic hold-down is introduced in this experimental series, see Fig. 1(c). It consists of a height-adjustable base ring below the specimen and a pneumatically controlled downholder on top, leaving enough space for the DIC technique. In order to obtain a low friction coefficient, a pressure of 1bar is used in the system and lubricant is applied to the contact surfaces to minimize friction. The contact area is approximately 1200mm^2 on each side of the specimen. As a result, the out-of-sheet-plane deformations are reduced to less than 0.3mm.

During the experiments, three-dimensional displacement fields in selected regions of the specimen are monitored by DIC using a stereo setup with eight 6.0MPx cameras with 75mm lenses, as shown in Fig. 1(a)(b). With the corresponding lighting system, consisting of three Fomex FL-B50 LED-panel lights with 1600lx on the upper and lower sides, a spatial resolution of approximately 80px/mm can be achieved. This allows analysis of the evolution of different strain fields on the specimen surface and will reveal localization phenomena of the full deformation field. For the correlation process, the software Istra4D by Dantec Dynamics GmbH and a subset size of 33px with a grid spacing of 11px are used. In contrast to the conventional method, where a regular grid with equidistant grid points is laid over the image of a reference camera, the present image correlation algorithm uses the 3D-position and tangential plane of the underlying object surface for each of the grid points on both specimen sides. This gives additional information in thickness direction through the distance change of opposite surface points and therefore the possibility to transform strain quantities not only within the tangential plane of a subset but in 3D-space. A straightforward comparison with numerical quantities on the curved surface of notches is therefore enabled. In addition, after the experiments, the fracture surfaces of the failed specimens are examined by scanning electron microscopy to elucidate fracture modes on the micro-scale.

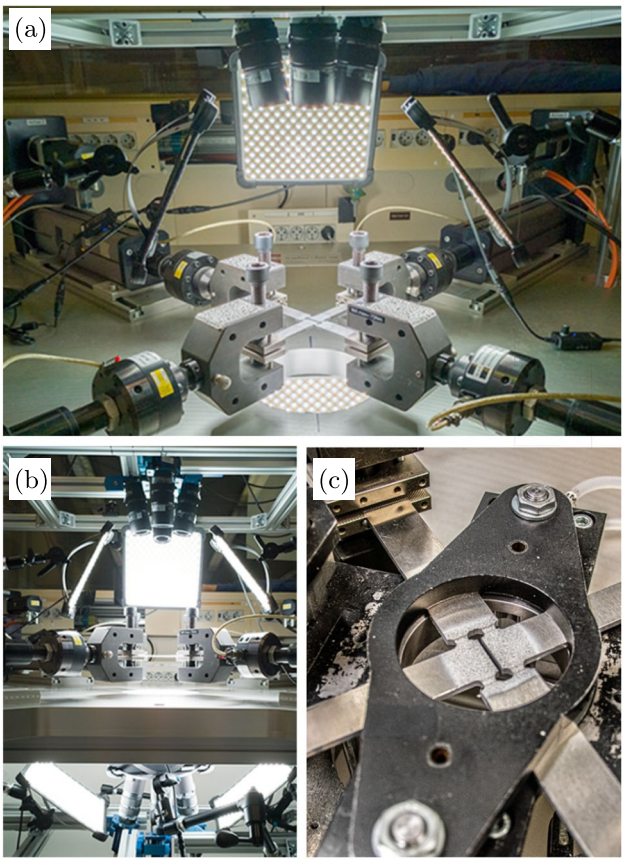

Fig. 1 Biaxial testing machine with DIC system and lighting: (**a**) machine overview, (**b**) double-sided 8-camera DIC setup and (**c**) pneumatic downholder for compression-dominated experiments

H-specimen

Geometries of suitable cruciform specimens have been proposed in [12] and the H-specimen (shown in Fig. 2) is tested in the present work in detail. The investigated material is the aluminum alloy EN AW6082 (AlSiMgMn) with the temper designation T6. The metal is supplied in 4mm thick sheets and its chemical composition is shown in Table 1.

The specimens are milled and have outer dimensions of 240mm×240mm. The depth of the notches is 1mm, which reduces the sheet thickness in the notch ground to 2mm (see Fig. 2(d)). The notches thus have a cross section of 6mm×2mm. The H-shaped central hole gives the specimen its name. The H-specimen has an easy to interpret relationship between the load ratio of the axes and the stress state in the notches due to their parallel orientation. Tensile loading in axis 1 results in a shear stress state and tensile loading in axis 2 corresponds to a tensile stress state with a high hydrostatic stress component caused by the notches. Compression loading in axis 2 results in a stress state with a significant hydrostatic pressure component. The simultaneous loading of both axes superimposes the respective stress states.

Furthermore, the force averages per axis

$$F_i = \frac{F_{i.1} + F_{i.2}}{2}, \tag{12}$$

as well as the relative displacement of the red dots in Fig. 2(a)

$$\Delta u_i = u_{i.1} - u_{i.2} \tag{13}$$

are introduced for a local displacement measure.

Numerical aspects

Numerical simulations were performed with the finite element program ANSYS. It is augmented by an user-defined material subroutine based on the continuum damage model and the numerical integration of the rate equations (for details, see [39]). Taking advantage of the symmetries, a quarter of the H-specimen is discretized by 7712 eight-node-hexahedrons of type Solid185 (Fig. 2(e)). The element size of a hexahedron in the notch region is set to about 0.1mm. Since the specimen has four numerically redundant regions due to four notches, the numerical results of a localizing simulation of an ideal quarter of the specimen are necessarily different from the results of the real experiments and are not directly comparable. In particular, experiments encounter stronger and earlier localization in notches with the largest material or geometric imperfections and less localization in the remaining notches. The numerical simulation does not reproduce this asymmetric effect, so in order to allow better comparability, an experimental mean value is formed as a

Table 1 Chemical composition of EN AW 6082 T6 aluminum alloy (% weight)

Material	Si	Fe	Cu	Mn	Mg	Cr	Zn	Ti	others	Al
EN AW 6082-T6	0.9	0.37	0.09	0.47	0.7	0.02	0.09	0.03	0.04	to balance

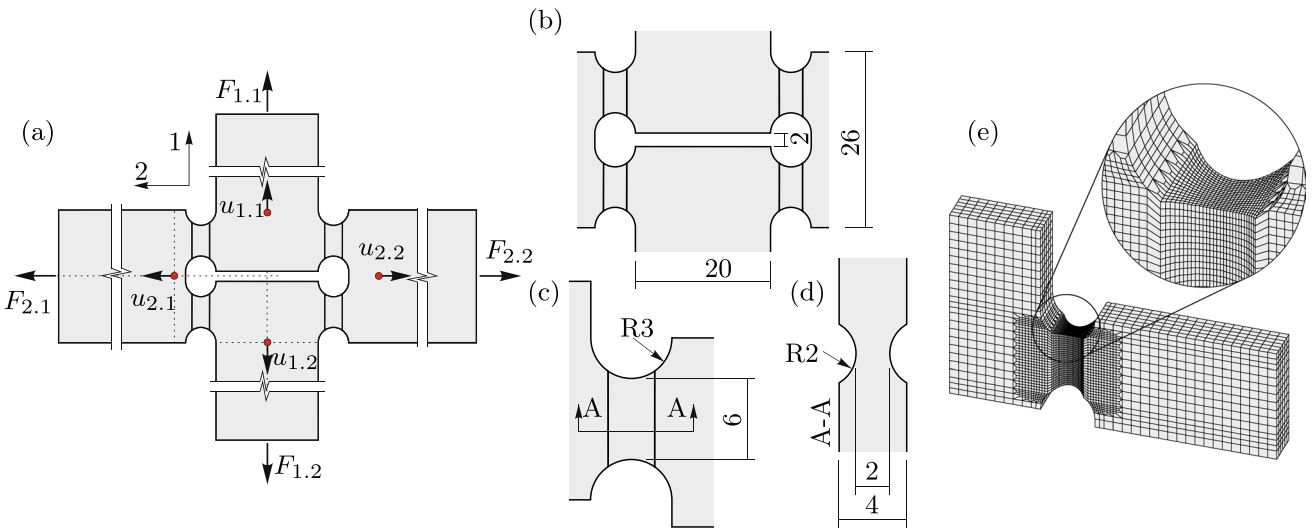

Fig. 2 (**a**) Notation for the H-specimen, (**b**)-(**d**) geometry details (dimensions in [mm]) and (**e**) finite element mesh

comparative value. For this purpose, the maximum values of the first principal strain of all four notches of an experiment are averaged, and this value is averaged again over all experiments with the same test routine. This resulting average value of the localization corresponds to a simultaneous and equally large localization in all four notches and is comparable with the numerical simulation. The qualitative distribution of the strains is generally very similar in all four notches. So, for comparison with the numerical results, a representative qualitative distribution with a mean value as the maximum can be used.

The numerical analysis is based on material parameters determined by inverse fitting load-displacement curves of uniaxial tension tests and proportional biaxial tests obtained through the DIC method. Initial elastic behavior is characterized by Young's modulus $E = 69{,}000MPa$ and Poisson's ratio $\nu = 0.29$. The deterioration of elastic properties by the evolution of damage is modeled by the parameters $\eta_1 ... \eta_4 = -10{,}000MPa$. In addition, the plastic hardening and current yield stress of the investigated aluminum alloy EN AW 6082-T6 is adequately described by Eq. 3 with the initial yield stress $c_o = 163.37MPa$, the hardening modulus $R_\infty = 74.93MPa$ and the hardening exponent $b = 8.66$. Damage softening is assumed to be modeled by Eq. 9 with the initial damage stress $\sigma_o = 295MPa$ and the softening modulus $H_1 = 400MPa$.

Results and discussion

To investigate the load path dependence of damage and failure mechanisms, different experiments are discussed and compared with failure under the same stress states but different loading histories. For this purpose, each load path is divided into different loading steps. The stress state in each step is controlled by the load ratio of the two specimen axes F_1/F_2. The respective load ratios result in different stress states with the corresponding inelastic deformation mechanisms. An important influence is the displacement at which a load step ends and the axis switch takes place. With this displacement, the influence of a non-proportional step on the overall load path of the experiment is defined, since it limits the inelastic deformations under a certain stress state.

The presented series covers four load paths with the H-specimen. A non-proportional load path consists of preloading in a first step with loading conditions that cause compression- and shear-dominated stress states until a high degree of deformation is reached. After a subsequent complete unloading, only axis 2 is loaded, and thus a stress state with a positive hydrostatic component is applied until failure occurs. A summary of all load cases and their numerical results can be found in Table 2.

Table 2 Summary of loading conditions and numerical results over the cross section at the time of axis switch after preloading and just before failure: mean values of stress triaxiality $\bar{\eta}$ and Lode parameter $\bar{\omega}$ as well as maximum inelastic equivalent strains

	F_1/F_2	$\bar{\eta}$	$\bar{\omega}$	γ_{max}	μ_{max}
(a) fracture	0/+1	0.65	-0.55	0.21	0.07
(b1) preload	1/-2	-0.30	0.40	1.13	0.07
(b2) fracture	0/+1	0.50	-0.65	1.21	0.07
(c1) preload	1/-1	-0.15	0.20	0.71	0.01
(c2) fracture	0/+1	0.55	-0.70	0.75	0.01
(d1) preload	1/0	0.10	-0.10	0.75	0.09
(d2) fracture	0/+1	0.50	-0.70	0.78	0.09

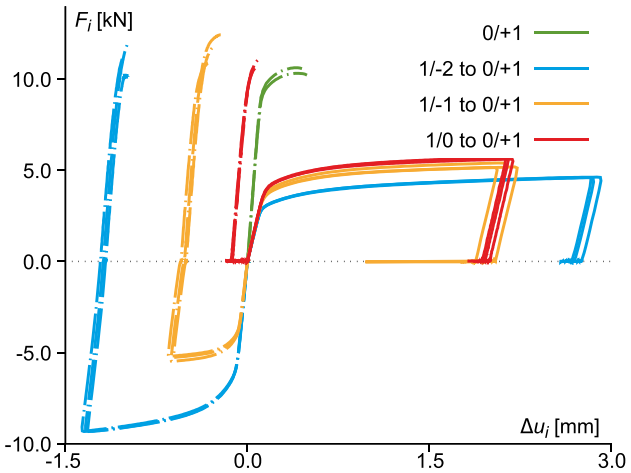

Fig. 3 Experimental load-displacement curves for final load ratio $F_1/F_2 = 0/+1$ with different compression or shear preloadings

Global forces and displacements

Figure 3 shows the forces F_i versus relative displacements Δu_i determined by the DIC method of load paths with an equal final load ratio of $F_1/F_2 = 0/+1$ leading to tensile behavior. The solid lines show quantities of axis 1, and the dash-dotted lines show quantities of axis 2.

The load-displacement curve for the proportional experiment 0/+1 is characterized by a linear increase in force up to $F_2 = 8.4kN$, a subsequent maximum force of $F_2 = 10.4kN$, and a small drop in force until failure at $\Delta u_2 = 0.47mm$.

In the first non-proportional load path (1/-2 to 0/+1), which corresponds to a stress state with a significant hydrostatic compression component, the point of axis switch is reached at $\Delta u_1 = 2.85mm$ with a load ratio of $F_1/F_2 = 1/-2$. This displacement corresponds to approximately 85% of the displacement at fracture of the corresponding proportional load path 1/-2. A significant reduction in stiffness and an increase in fracture displacement compared to the 0/+1 load case are noted. The onset of inelastic deformations

is at $F_1 = -0.5F_2 = 2.7kN$ and the subsequent evolution of deformations up to the axis switch is characterized by a very small increase in forces. At $F_1 = -0.5F_2 = 4.6kN$ the axis switch is reached and then both axes are completely unloaded with a decrease in displacement. In the following final load step, only axis 1 is pulled and a large linear path is obtained with a slight increase in stiffness compared to unloading. Then, only small inelastic deformations take place until failure occurs after an additional displacement of about $\Delta u_2 = 0.20mm$ and a maximum force of $F_2 = 11.1kN$.

The second experiment with the non-proportionally loaded specimen (1/-1 to 0/+1) has in its first load step forces of $F_1 = -F_2$ and switches at a displacement of $\Delta u_1 = 2.10mm$ (about 70% of the fracture displacement) to unloading. Axis 2 experiences a negative displacement of $\Delta u_2 = -0.60mm$. The linear slope is flatter for axis 2 and steeper for axis 1 than during load ratio 1/-1, whereby both curves are flatter than in the experiment with the proportionally loaded specimen. The onset of inelastic deformations is at approximately $F_1 = -F_2 = 3.6kN$ and the hardening behavior is similar to that of the load ratio 1/-2. The final proportional loading is again similar to the only proportionally loaded specimen, whereas after a displacement increment of about $\Delta u_2 = 0.25mm$, the maximum force of $F_2 = 11.7kN$ is reached.

The third load path (1/0 to 0/+1) involves an axis switch after a shear load 1/0 up to the displacement of $\Delta u_1 = 2.16mm$, which corresponds to about 90% of the fracture displacement. During this step, only axis 1 is loaded, and therefore axis 2 experiences a negative displacement of $\Delta u_2 = -0.06mm$. The slope of axis 1 is almost the same for experiments 1/0 and 1/-1, only the onset of inelastic deformations is slightly later for 1/0. The linear progression of axis 2 in the last load step now runs with a slightly reduced slope compared to 0/+1. With a displacement increment of $\Delta u_2 = 0.21mm$, only small inelastic deformations are formed before failure occurs under the maximum force of $F_2 = 10.7kN$.

The results of numerical simulations of these experiments are displayed with the experimental data in Fig. 4. The simulation with proportional loading (a) shows no differences in the linear elastic region and the inelastic deformations up to failure agree very well too. In the three simulations with a non-proportional load path, the first loading up to the axis switch is calculated very well, with only minor deviations occurring in the prediction of the onset of inelastic deformations. For the simulation (b), the final load step coincides very well, only the forces at the time of failure are slightly overestimated. In (b) and (c), slight deviations appear in the linear increase of the last loading step, but the qualitative agreement is excellent. The non-proportional load (d) is almost exactly on the experimental results and only marginal deviations can be detected. The numerical simulations predict the global behavior of the conducted experiments very well.

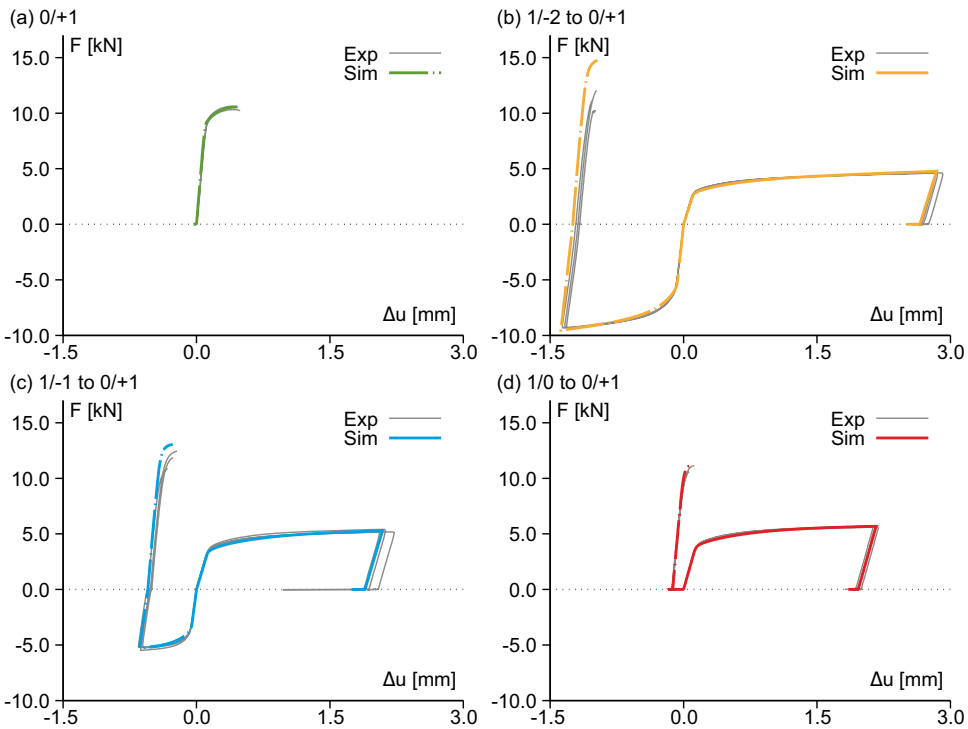

Fig. 4 Experimental and numerically predicted load-displacement curves for final loading ratio $F_1/F_2 = 0/+1$ and different compression or shear preloadings

Local strains

To investigate the local deformation behavior, strain results from the DIC system are used, see Fig. 5. At the time of axis switch, the first principal strain values are compared. Just before failure, strains are dominated by the large shear strains at the axis switch. Therefore, here only the increment of true strain in 2-direction (defined in Fig. 2) between the time of full unloading and just before failure is used to allow better comparability. For the proportional load path (a), the strain in the tension direction appears in a widespread, vertical band that is offset from the axis of symmetry and reaches maxima of 0.15. In the numerical simulation, a wider band with already visible signs of necking at the edges and maxima of 0.14 are calculated.

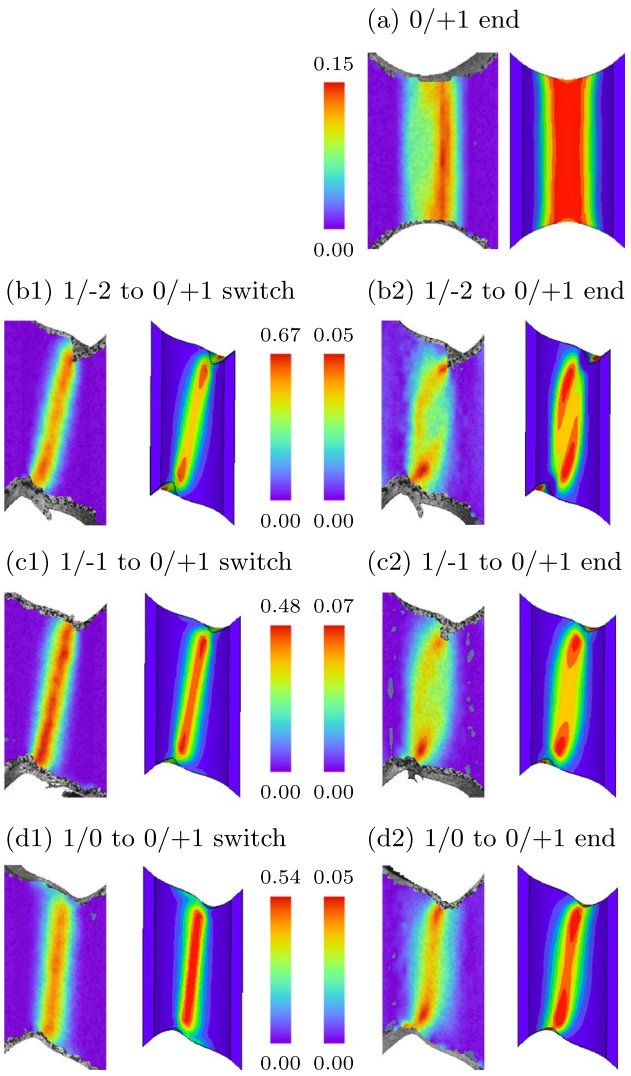

Fig. 5 First principal strains of the notch surface at the axis switch (left column) for the DIC measurements (respectively left) and the numerical simulations (respectively right) as well as true strain increment of the tensile loading (right column) with load ratio 0/+1 in 2-direction (defined in Fig. 2(a))

In the load case (b1), at the axis switch true principal strains of up to 0.63 are formed in the experiment. They are distributed in an inclined band and the maxima occur near the edge of the notch. Remarkable compression of the notch and the formation of indentations on the upper and lower sides of the radii are clearly visible here as a result of the compression loading. In the numerical simulation, this diagonal localization band and the location of the maxima are also predicted. A strain increment in the 2-direction of 0.05 is observed in the final tensile loading step (b2). The maxima form at the indentations created by the compression preloading in a vortex-shaped distribution and extend to the opposite side of the notch. This qualitative distribution and maxima of 0.05 are also calculated in the numerical simulation, although the location of the maxima and position of the vortices is slightly offset towards the center. In comparison, the strain to failure in two-direction is here only 33% of the simulation with only proportional loading.

In the second non-proportional load case (c1), again an inclined narrow band with maxima of 0.48 is observed. This smaller strain maximum is a result of the lower percentage of fracture displacement at axis switch. The simulation also predicts this distribution with maxima of 0.45. From unloading to failure (c2), maxima again occur at the geometric indentations due to compression loading, although the maxima are now larger at 0.07 and the band created by the vortices is narrower and forms an S-shape. The simulation calculates a S-shape as well and reaches maxima of 0.07. The strain to failure in 2-direction is only about 50% of that one after corresponding proportional loading.

As a result of the load ratio 1/0 in (d1), an only slightly tilted and more evenly distributed localized band is formed. The experimental maxima of 0.49 are lower than in the numerical simulation of 0.54, although the qualitative distribution agrees very well. In the 0/+1 increment of this experiment, the distribution of strain develops in a S-shape with maxima at the edge of 0.05. The corresponding numerical simulation also calculates maxima of 0.05 but again predicts larger strains in the middle region of the S-shaped band. Here, strain to failure in 2-direction is again 33% of that one after proportional loading.

In summary, the experimental results are well reproduced by the numerical simulations and the deviations are overall less than 10%. Furthermore, a remarkable difference is found in the last strain increment in 2-direction up to failure. The maximum strains in non-proportional load paths are reduced by up to one third compared to the proportional load case, and their distribution is also strongly changed by the pre-deformations. A clear load path dependency is visible as a result of those large pre-deformations in reduced failure strains.

Stress states

The stress state in this series is represented by the stress triaxiality η and the Lode parameter ω.

The evolution of stress state within a load case is displayed in Fig. 6. In (a) the mean value of stress intensity $\bar{\sigma}_I$, with the stress intensity being defined as

$$\sigma_I = \max\left(\left|T_1 - T_2\right|, \left|T_2 - T_3\right|, \left|T_3 - T_1\right|\right) \quad (14)$$

in terms of the principal Kirchhoff stress components, is displayed over the mean value of von Mises equivalent strain $\bar{\varepsilon}_{eq}$ in the cross section of a notch. Here, the residual stress after unloading and a reduction of equivalent strain within the last load step through a change in loading direction become apparent. The evolution of the mean stress triaxiality $\bar{\eta}$ and mean Lode parameter $\bar{\omega}$ over the mean value of the equivalent stress in the cross section is shown in (b). Overall, the mean value of stress triaxiality and Lode parameter change only slightly throughout one load step. The geometric changes lead to a decrease of initially positive values and an increase of initially negative or zero values. In contrast, the Lode parameter always decreases slightly for the four investigated load paths. After preloading, a jump in stress state in the direction of that one of the corresponding proportional simulation is visible.

The spatial distribution of stress triaxiality in a notch at the time after pre-loading and just before fracture is displayed in Fig. 7. Here results on the surface (S), a longitudinal section (L) and a cross section (C) are displayed. In particular, for the simulation (0/+1 end), a rather homogeneous distribution with the influence of the geometry is numerically predicted ($0.4 \leq \eta \leq 0.8$). At the time of axis switch (b1), values between $-0.50 \leq \eta \leq -0.25$ are calculated.

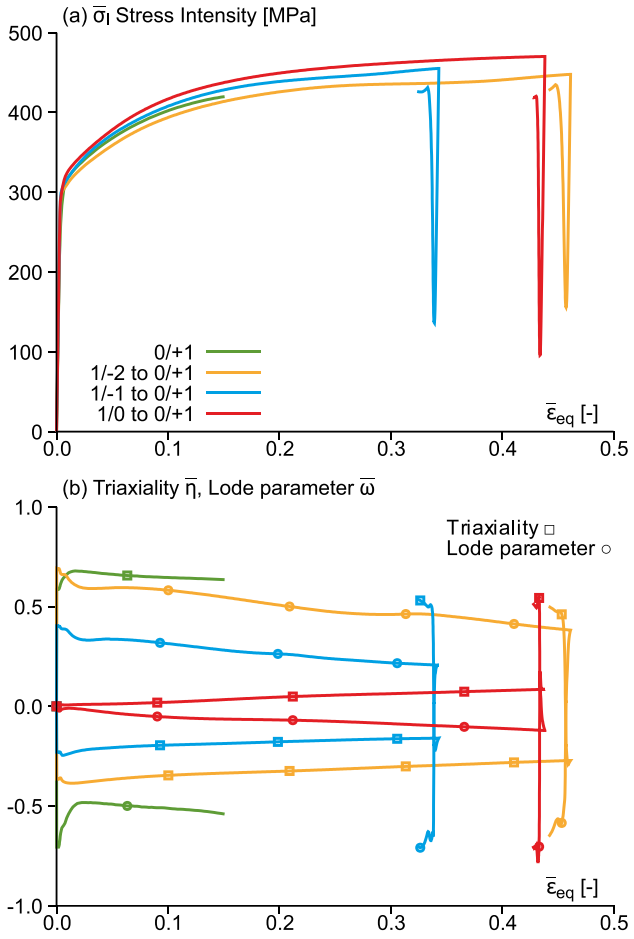

Fig. 6 Numerically calculated evolution of mean stress intensity over mean equivalent strain (a) as well as mean stress triaxiality and Lode parameter over mean equivalent strain (b) in the cross section of the notch

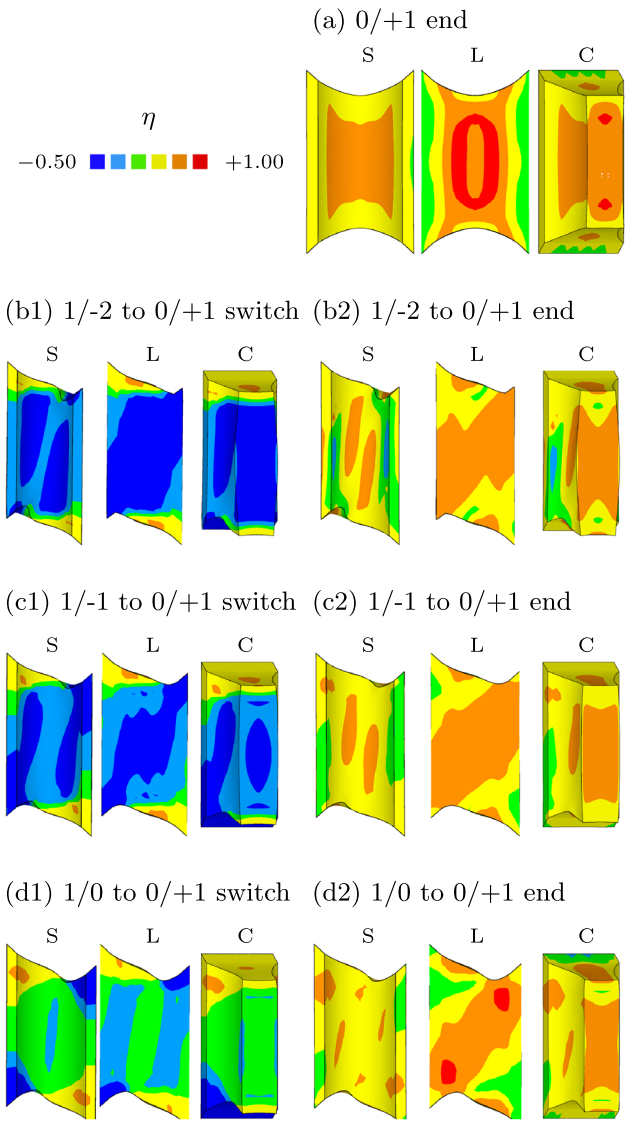

Fig. 7 Stress triaxiality η: S – surface, L – longitudinal section, C – cross section

These values rise to $\eta = 0.7$ in the cross section's center just before fracture (b2). But clear differences in comparison with the proportional load case are visible due to lower values in the distribution.

This qualitative tendency continues in (c1). Here values between $-0.33 \leq \eta \leq -0.05$ are initially reached and then at the end of the 0/+1 load step an increase up to $\eta = 0.75$ in the center is calculated. In the last simulation with the non-proportionally loaded specimen (1/0 to 0/+1), the cross section at the axis change (d1) has a nearly homogeneous distribution of the stress triaxiality of approximately $\eta = 0.0$. At the time of (d2), this distribution changes with values of up to $\eta = 0.75$. In this series, a strong change in the stress triaxiality takes place and a large bandwidth of stress states in the first load step is covered. At the same time, large pre-deformations have a visible but relatively small influence on the stress state at the time of fracture, resulting in only slightly lower values compared to the proportional experiment.

When the spatial distribution of the Lode parameter ω is compared at two points in time (Fig. 8), a clear difference can be seen between the first and last load step. In the proportionally loaded simulation (a), a distribution with larger gradients over the cross section from $\omega = 0.0$ at the long edges up to $\omega = -1.0$ at the short edges is calculated. On the other hand, the high compression stress results in positive values of the Lode parameter in (b1). Under the final load ratio 0/+1, the distribution develops values up to $\omega = -1.0$ again, but areas with $\omega = 0.0$, as shown in (a), vanish.

At the axis switch of (c1), the qualitative distribution is similar to (b1), but the range of values has been slightly shifted in the negative direction for the cross section. This drops to $\omega = -1.0$ at the final load ratio, with distributions similar to (a) and (b1). In the last non-proportional path after load ratio 1/0, the Lode parameter drops again compared to the other two paths, reaching only values in the slightly negative range around $\omega = 0.0$. Here too, at the time of failure, the Lode parameter drops to $\omega = -1.0$, whereby the gradient over the cross section is smaller.

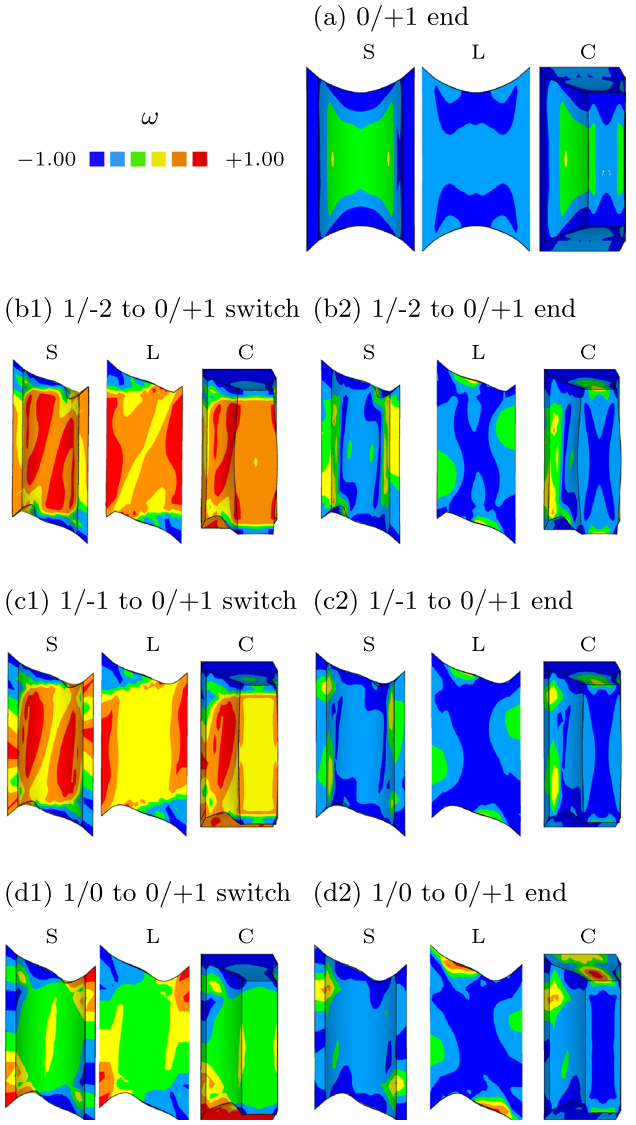

Fig. 8 Lode parameter ω: S – surface, L – longitudinal section, C – cross section

Plastic and damage equivalent strains

The spatial distribution of the plastic equivalent strain γ is displayed in Fig. 9. For the final load ratio of 0/+1, a vertical band with maxima distributed in an ellipsoidal shape forms around the notch center ($\gamma = 0.21$). Due to higher stress triaxialities, values in the center are lower, down to $\gamma = 0.13$. In the first non-proportional load case, large plastic equivalent strains are already present at the axis switch with a maximum of $\gamma = 1.13$ near the double-curved radius. The strain is distributed in a slightly inclined band in the orientation of the first principal strain, stretching on both sides of the notch with smaller values of around $\gamma = 0.95$. Before fracture (b2), only small additional inelastic deformations are present (see Fig. 4) and form in a very narrow band. This behavior also applies to the simulation of the second non-proportionally loaded specimen, whereas here the localization band is more vertical and the values at the axis switch (c1) increase from $\gamma = 0.71$ to $\gamma = 0.78$ at the time just before failure (c2). In the last load case (d1), the localization becomes even more vertical and the strain band on the upper and lower sides of the notch disappears. Just before failure (d2), only a slight increase to $\gamma = 0.78$ can be seen. The first load step is the dominant step in this series and largely determines the location and magnitude of the equivalent plastic strain at the time of failure. Its distribution aligns with the first principal strain and the maximum values form near the surface. The ratio of maximum values between the three non-proprtional load

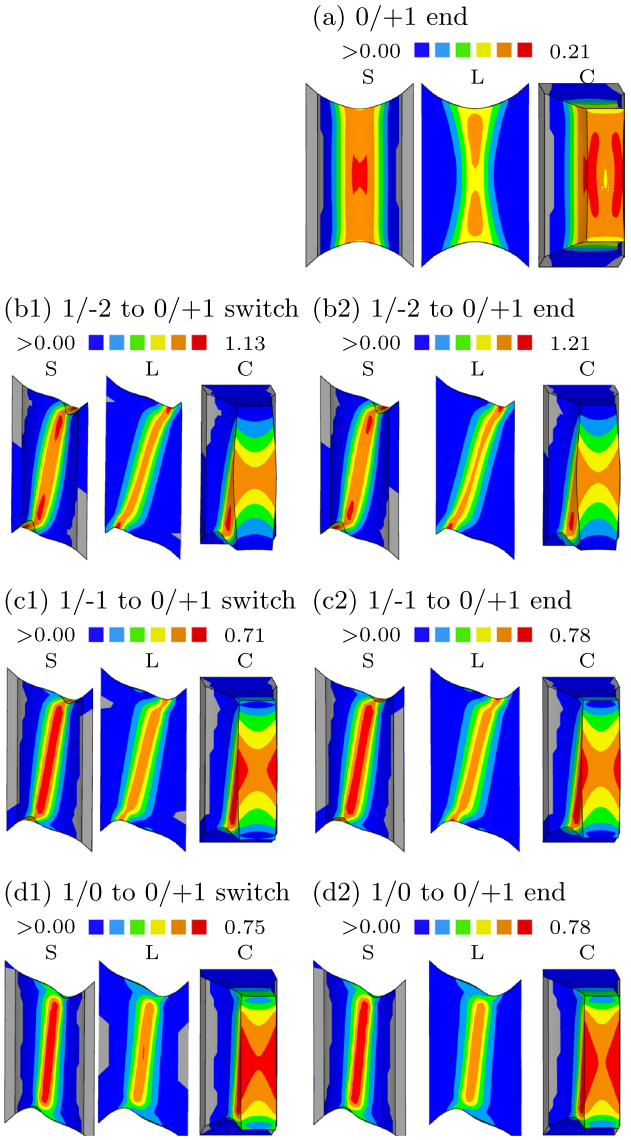

Fig. 9 Equivalent plastic strain γ: S – surface, L – longitudinal section, C – cross section

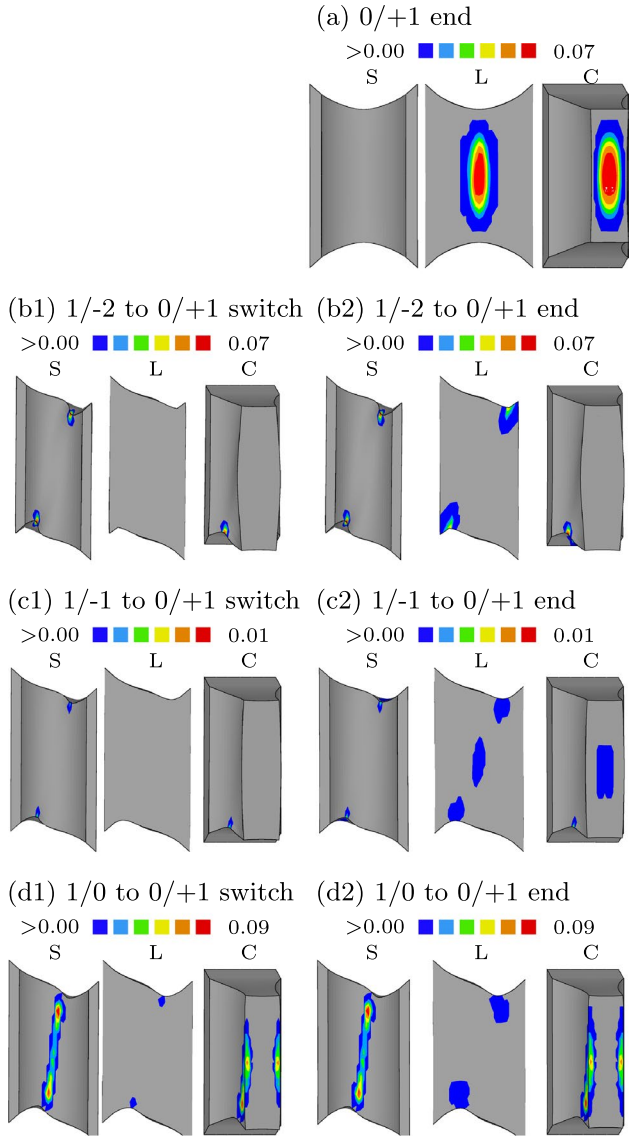

Fig. 10 Equivalent damage strain μ: S – surface, L – longitudinal section, C – cross section

cases after preloading is quite similar to the ratio of principal strains in Fig. 4, except for (b1), where two small regions with a high strain deviate from this ratio.

In the proportional load case 0/+1, for the damage equivalent strain μ in Fig. 10, a maximum of $\mu = 0.07$ is found at the center of the notch with an ellipsoidal distribution within the maximum equivalent plastic strain in Fig. 9(a). Consequently, plasticity and damage have the tendency to develop in different areas of high positive stress triaxialities. At the axis switch of (b1), only small local damage developments are calculated directly in the geometric indentations on the upper and lower faces next to overall high negative triaxialities. In the central region, triaxialities of around $\eta = -0.5$ are present with no damage evolution. The specimen thus may fail despite a predominantly existing triaxiality below $\eta = -0.33$, because damage evolution takes place in areas with a triaxiality of $\eta = 0.0$ to $\eta = 0.25$ at the surface. The maxima in the four predicted damaged locations reach values of $\mu = 0.07$. Shortly before fracture, the magnitude of maxima does only change marginally, but in the longitudinal section, two larger areas form in between with values of $\mu = 0.07$.

In the load case (1/-1 to 0/+1 switch), this damage development at the indentations is also present, but at low values of $\mu = 0.01$. At the time of failure (c2), on the other hand, in addition to the merging into two bands, small damage strains occur in the central area ($\mu = 0.01$), similar to the proportional load case. Furthermore, as the pre-deformation of this

load case is small, additional damage evolution occurs not only in the damaged areas of the first load step but also in the central areas like in the proportional tension load case.

The fourth load case (1/0 to 0/+1 switch) results in the formation of a slightly inclined band on the surface with $\mu = 0.09$, which is similar to the equivalent plastic strain γ in Fig. 9(d1). The maxima are located near the indentations and run at the center just below the surface. A coincidence in the location of predicted small damage strains and large plastic strains might be a possible cause for the onset of failure. Initiations of minor damage development can also be seen on the top and bottom surfaces of the notch. After the axis switch, the failure point is reached as soon as the damage developments on the upper and lower sides grow into the longitudinal section. Again, no significant additional damage is predicted at the surface. Further evolution of damage takes place in the longitudinal section.

In summary, at the axis switch under shear and compression loading, damage is determined exclusively on the surface, which propagates in the final load step under the high hydrostatic tensile stress component. The final distribution, on the other hand, depends on the preliminary damage in the first step. If significant damage strains have already taken place before the axis switch, damage will continue to develop in these areas and may be the cause of failure there. But in the case of minor damage evolution during pre-deformation, evolution takes place below the notch surface, where high stress triaxialities are present. This provides a clear indication of the load path dependence of damage and failure and enables a systematic investigation.

Fracture behavior

The images in Fig. 11 show fractured specimens after all load paths and the results of the examination of fracture surfaces with the scanning electron microscope (SEM). The pictures clearly show the tendency for fracture lines to develop from a vertical one after proportional loading to an inclined one due to non-proportional loading. In this process, the angle to the vertical slightly decreases from (b) to (d), showing good agreement with the distributions of principal strains (Fig. 5) as well as the inelastic equivalent strains (Figs. 9, 10). The first SEM image (Fig. 11(a)) clearly shows void formation with numerous large craters, as well as an overall flat topology for the experiment with proportional loading and a high positive triaxiality (Fig. 7(a)).

In the non-proportional load path (1/-2 to 0/+1), a fissuring of the fracture surface is visible, indicating less ductile material behavior. Here, the hardening effect of dislocation processes may facilitate this development. Furthermore, only small pores are visible on the small terraces oriented perpendicular to the fracture surface. They developed presumably during the high hydrostatic stress state during the last load step.

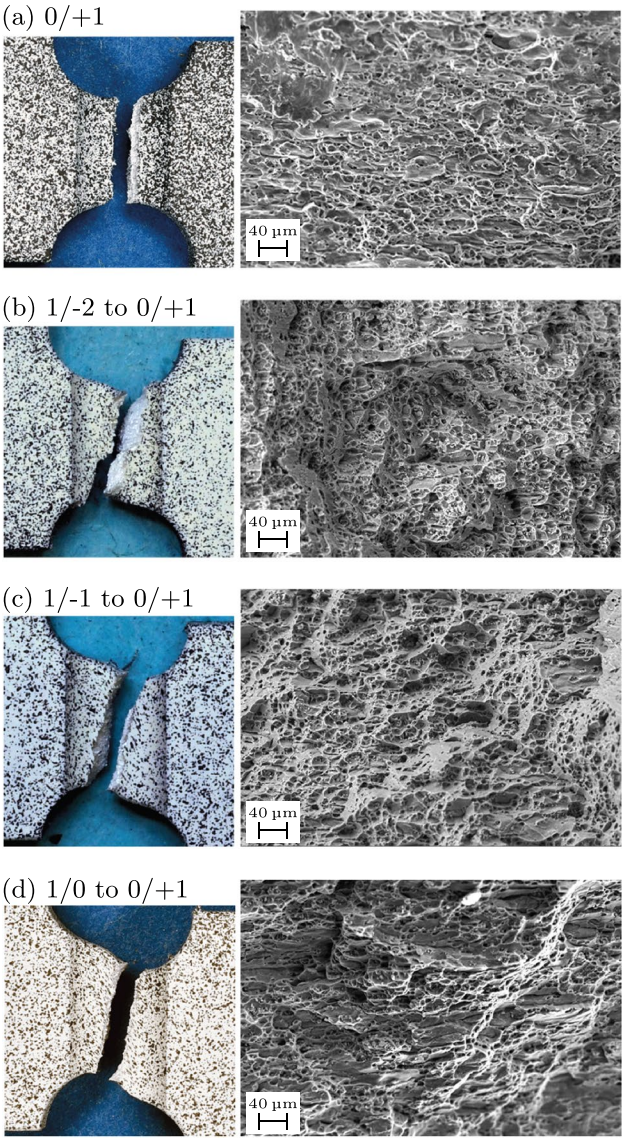

Fig. 11 Fracture lines and scanning electron microscopy (SEM) pictures of the fracture surfaces

The next load case (1/-1 to 0/+1) leads to a reduction in ductility as well, although it is less pronounced. Again, smaller pores are present and the orientation of terraces is similar. The strains at the axis switch (see Fig. 5(c1)) are significantly lower than in the load case (1/-2 to 0/+1), which may explain why the ductility reduction is smaller. For the load case with shear pre-deformation (d), sheared layers with parallel orientation to the fracture surface are visible. Additionally, the formation of small pores and craters in all orientations to the fracture surface is visible. In all images of non-proportionally loaded specimens, the less ductile character of the force-displacement diagrams in Fig. 3 is apparent. The influence of different stress states in a non-proportional load path is mirrored in the corresponding micro-mechanisms.

Conclusion

In this paper, the influence of different load paths on damage and fracture behavior of aluminum alloys was investigated in detail. Various experiments and corresponding numerical simulations with the biaxially loaded H-specimen were performed with focus on different highly preloaded compression and shear stress states. With the experimental methodology, it is feasible to investigate extreme changes in stress triaxialities ($-0{,}5$ to $+0{,}8$) with soft transitions in an experimental manner. In order to prevent buckling of the specimen under high compression loading in metal sheets, the experimental procedure was facilitated with a pneumatic downholder. It could be shown that pre-deformations with shear and compression stress states lead to reduced ductility of the material behavior. As a consequence, even the evolution of only small local damage strains could cause the initiation of the failure process. Additionally, a change in the location of damage evolution and therefore, a possibly different location of failure initiation can be noted under the final tensile loading. Large pre-deformations with shear or compression loading shift final damage evolution to the pre-damaged surface of the notches. The experimentally observed micro-structure on the fracture surfaces seems to reflect the numerically predicted stress states with corresponding damage mechanisms. This is even true for the combination of micro-shear-cracks and micro-pore formation corresponding to the history of the stress states in non-proportional load paths. The constitutive model with the presented parameterization is capable of accurately predicting the complex material behavior under a variety of load paths. The presented methodology is very well suited to investigate non-proportional load paths with high compressive and shear pre-loading and thus, validation of stress-state-dependent material models for industrial forming applications is possible.

Acknowledgements The financial support of the Deutsche Forschungsgemeinschaft DFG is gratefully acknowledged. The technical support of Wolfgang Saur (Universität der Bundeswehr München, Werkstoffe das Bauwesens, Germany) is also gratefully acknowledged. Furthermore, the authors thank Prof. Ingo Ehrlich (Ostbayerische Technische Hochschule Regensburg, Labor für Faserverbundtechnik, Germany) for providing the pneumatic downholder.

Funding Open Access funding enabled and organized by Projekt DEAL. Funded by the Deutsche Forschungsgemeinschaft DFG (German Research Foundation) — 322157331.

Declarations

Conflict of Interests The authors declare that they have no conflict of interest.

Open Access This article is licensed under a Creative Commons Attribution 4.0 International License, which permits use, sharing, adaptation, distribution and reproduction in any medium or format, as long as you give appropriate credit to the original author(s) and the source, provide a link to the Creative Commons licence, and indicate if changes were made. The images or other third party material in this article are included in the article's Creative Commons licence, unless indicated otherwise in a credit line to the material. If material is not included in the article's Creative Commons licence and your intended use is not permitted by statutory regulation or exceeds the permitted use, you will need to obtain permission directly from the copyright holder. To view a copy of this licence, visit http://creativecommons.org/licenses/by/4.0/.

References

1. Brocks W, Sun D-Z, Hönig A (1995) Verification of the transferability of micromechanical parameters by cell model calculations with visco-plastic materials. Int J Plast 11 (8):971–989. https://doi.org/10.1016/S0749-6419(95)00039-9
2. Chew HB, Guo TF, Cheng L (2006) Effects of pressure-sensitivity and plastic dilatancy on void growth and interaction. Int J Solids Struct 43(21):6380–6397. https://doi.org/10.1016/j.ijsolstr.2005.10.014
3. Kim J, Gao X, Srivatsan TS (2003) Modeling of crack growth in ductile solids: a three-dimensional analysis. Int J Solids Struct 40(26):7357–7374. https://doi.org/10.1016/j.ijsolstr.2003.08.022
4. Brünig M, Hagenbrock V, Gerke S (2018) Macroscopic damage laws based on analysis of microscopic unit cells. Z Angew Math Mech 98(2):181–194. https://doi.org/10.1002/zamm.201700188
5. Gao X, Zhang G, Roe CA (2010) Study on the effect of the stress state on ductile fracture. Int J Damage Mech 19(1):75–94. https://doi.org/10.1177/1056789509101917
6. Bai Y, Wierzbicki TA (2008) New model of metal plasticity and fracture with pressure and Lode dependence. Int J Plast 24(6):1071–1096. https://doi.org/10.1016/j.ijplas.2007.09.004
7. Driemeier L, Brünig M, Micheli G, Alves M (2010) Experiments on stress-triaxiality dependence of material behavior of aluminum alloys. Mech Mater 42(2):207–217. https://doi.org/10.1016/j.mechmat.2009.11.012
8. Bonora N, Gentile D, Pirondi A, Newaz G (2005) Ductile damage evolution under triaxial state of stress: theory and experiments. Int J Plast 21(5):981–1007. https://doi.org/10.1016/j.ijplas.2004.06.003
9. Miyauchi K (1984) Proposal of a planar simple shear test in sheet metals. Sci Pap Inst Phys Chem Res 78(3):27–40
10. Arcan M, Hashin Z, Voloshin A (1978) Method to produce uniform plane-stress states with applications to fiber-reinforced materials. Exp Mech 18(4):141–146. https://doi.org/10.1007/BF02324146
11. Dunand M, Mohr D (2011) Optimized butterfly specimen for the fracture testing of sheet materials under combined normal and shear loading. Eng Fract Mech 78(17):2919–2934. https://doi.org/10.1016/j.engfracmech.2011.08.008
12. Gerke S, Adulyasak P, Brünig M (2017) New biaxially loaded specimens for the analysis of damage and fracture in sheet metals. Int J Solids Struct 110-111:209–218. https://doi.org/10.1016/j.ijsolstr.2017.01.027
13. Kulawinski D, et al. (2011) Characterization of stress–strain behavior of a cast TRIP steel under different biaxial planar load ratios. Eng Fract Mech 78(8):1684–1695. https://doi.org/10.1016/j.engfracmech.2011.02.021
14. Brünig M, Brenner D, Gerke S (2015) Stress state dependence of ductile damage and fracture behavior: Experiments and numerical simulations. Eng Fract Mech 141:152–169. https://doi.org/10.1016/j.engfracmech.2015.05.022
15. Brünig M, Zistl M, Gerke S (2019) In modeling of damage of ductile materials. In: Altenbach H, Öchsner A (eds) State of the

Art and Future Trends in Material Modeling, vol 100. Springer International Publishing, Cham, pp 49–78
16. Roth CC, Mohr D (2016) Ductile fracture experiments with locally proportional loading histories. Int J Plast 79:328–354. https://doi.org/10.1016/j.ijplas.2015.08.004
17. Hartmann S, Gilbert RR, Sguazzo C (2018) Basic studies in biaxial tensile tests. GAMM-Mitt 41(1):1–14. https://doi.org/10.1002/gamm.201800004
18. Boger RK, Wagoner RH, Barlat F, Lee MG, Chung K (2005) Continuous, large strain, tension/compression testing of sheet material. Int J Plast 21(12):2319–2343. https://doi.org/10.1016/j.ijplas.2004.12.002
19. Steglich D, Tian X, Bohlen J, Kuwabara T (2014) Mechanical testing of thin sheet magnesium alloys in biaxial tension and uniaxial compression. Exp Mech 54(7):1247–1258. https://doi.org/10.1007/s11340-014-9892-0
20. Zaplatić A, Tomičević Z, Čakmak D, Hild F (2022) Improvement of the arcan setup for the investigation of thin sheet behavior under shear loading. Exp Mech 62(2):313–332. https://doi.org/10.1007/s11340-021-00762-1
21. Tarigopula V, Hopperstad OS, Langseth M, Clausen AH (2008) Elastic-plastic behaviour of dual-phase, high-strength steel under strain-path changes. Eur J Mech A Solids 27(5):764–782. https://doi.org/10.1016/j.euromechsol.2008.01.002
22. Basu S, Benzerga AA (2015) On the path-dependence of the fracture locus in ductile materials: Experiments. Int J Solids Struct 71:79–90. https://doi.org/10.1016/j.ijsolstr.2015.06.003
23. Gardey B, Bouvier S, Richard V, Texture B (2005) Dislocation structures observation in a dual-phase steel under strain-path changes at large deformation. Mater Sci Eng Bacroix A 400-401:136–141. https://doi.org/10.1016/j.msea.2005.01.066
24. Cortese L, Nalli F, Rossi MA (2016) Nonlinear model for ductile damage accumulation under multiaxial non-proportional loading conditions. Int J Plast 85:77–92. https://doi.org/10.1016/j.ijplas.2016.07.003
25. van Riel M (2009) Strain path dependency in sheet metal: Experiments and models. Ph.D. thesis, University of Twente
26. Fincato R., Tsutsumi S. (2019) Numerical modeling of the evolution of ductile damage under proportional and non-proportional loading. Int J Solids Struct 160:247–264. https://doi.org/10.1016/j.ijsolstr.2018.10.028
27. Zhuang X, Wang T, Zhu X, Calibration Z (2016) Application of ductile fracture criterion under non-proportional loading condition. Eng Fract Zhao Mech 165:39–56. https://doi.org/10.1016/j.engfracmech.2016.08.021
28. Baral M, Korkolis YP (2021) Ductile fracture under proportional and non-proportional multiaxial loading. Int J Solids Struct 210-211:88–108. https://doi.org/10.1016/j.ijsolstr.2020.11.011
29. Korkolis YP, Kyriakides S (2009) Path-dependent failure of inflated aluminum tubes. Int J Plast 25(11):2059–2080. https://doi.org/10.1016/j.ijplas.2008.12.016
30. van Riel M, van den Boogaard AH, Huetink H, Juster N, Rosochowski A (eds) (2006) Non-proportional tension-shear experiments in a biaxial test facility. In: Juster N, Rosochowski A (ed) ESAFORM 2006, Publishing House AKAPIT, Austria, p 323-326
31. Wang J, Chow CL (1989) Mixed mode ductile fracture studies with nonproportional loading based on continuum damage mechanics. J Eng Mater Technol 111(2):204–209. https://doi.org/10.1115/1.3226455
32. Chow CL, Lu TJ (1992) An analytical and experimental study of mixed-mode ductile fracture under nonproportional loading. Int J Damage Mech 1 (2):191–236. https://doi.org/10.1177/105678959200100203
33. Brünig M, Gerke S, Zistl M (2019) Experiments and numerical simulations with the H-specimen on damage and fracture of ductile metals under non-proportional loading paths. Eng Fract Mech 217:106531. https://doi.org/10.1016/j.engfracmech.2019.106531
34. Gerke S, Zistl M, Bhardwaj A, Brünig M (2019) Experiments with the X0-specimen on the effect of non-proportional loading paths on damage and fracture mechanisms in aluminum alloys. Int J Solids Struct 163:157–169. https://doi.org/10.1016/j.ijsolstr.2019.01.007
35. Brünig M, Zistl M, Gerke S (2020) Biaxial experiments on characterization of stress-state-dependent damage in ductile metals. Prod Eng 14(1):87–93. https://doi.org/10.1007/s11740-019-00930-2
36. Brünig M, Zistl M, Gerke S (2021) Numerical analysis of experiments on damage and fracture behavior of differently preloaded aluminum alloy specimens. Metals 11(3):381. https://doi.org/10.3390/met11030381
37. Gerke S, Zistl M, Brünig M (2020) Experiments and numerical simulation of damage and fracture of the X0-specimen under non-proportional loading paths. Eng Fract Mech 224:106795. https://doi.org/10.1016/j.engfracmech.2019.106795
38. Brünig M (2003) An anisotropic ductile damage model based on irreversible thermodynamics. Int J Plast 19(10):1679–1713. https://doi.org/10.1016/S0749-6419(02)00114-6
39. Brünig M (2003) Numerical analysis of anisotropic ductile continuum damage. Comput Methods Appl Mech Eng 192(26-27):2949–2976. https://doi.org/10.1016/S0045-7825(03)00311-6
40. Brünig M, Chyra O, Albrecht D, Driemeier L, Alves MA (2008) Ductile damage criterion at various stress triaxialities. Int J Plast 24(10):1731–1755. https://doi.org/10.1016/j.ijplas.2007.12.001
41. Bao Y, Wierzbicki T (2004) On fracture locus in the equivalent strain and stress triaxiality space. Int J Mech Sci 46(1):81–98. https://doi.org/10.1016/j.ijmecsci.2004.02.006
42. Achouri M, Germain G, Dal Santo P, Saidane D (2013) Experimental characterization and numerical modeling of micromechanical damage under different stress states. Mater Des 50:207–222. https://doi.org/10.1016/j.matdes.2013.02.075
43. Voce E (1955) A practical strain-hardening function. Metall 51:219–226

Publisher's note Springer Nature remains neutral with regard to jurisdictional claims in published maps and institutional affiliations.